

Topological Control of Chirality and Spin with Structured Light

Light Mkhumbuza,¹ Pedro Ornelas,¹ Angela Dudley,¹ Isaac Nape,^{1,*} and Kayn A. Forbes^{2,†}

¹*School of Physics, University of the Witwatersrand, Private Bag 3, Wits 2050, South Africa*

²*School of Chemistry, University of East Anglia, Norwich Research Park, Norwich NR4 7TJ, United Kingdom*

Structured light beams with engineered topological properties offer a powerful means to control spin angular momentum (SAM) and optical chirality, key quantities shaped by spin–orbit interaction (SOI) in light. Such effects are typically regarded as emerging only through light–matter interactions. Here, we show that higher-order Poincaré modes, carrying a tunable Pancharatnam topological charge ℓ_p , enable precise control of SOI purely from the intrinsic topology of the light field, without requiring any material interface. In doing so, we reveal a free-space paraxial optical Hall effect, where modulation of ℓ_p drives spatial separation of circular polarization states – a direct signature of SOI in a regime previously thought immune to such behaviour. Our analysis identifies two propagation-induced topological mechanisms underlying this effect: differential Gouy phase shifts between orthogonal components, and radial divergence of the beam envelope. These results overturn the common view that spin-orbit effects in free space require non-paraxial conditions, and establish a broadly tunable route to generating and controlling chirality and SAM without tight focusing. This approach provides new opportunities for optical manipulation, chiral sensing, and high-dimensional photonic information processing.

I. INTRODUCTION

Light’s spin and orbital angular momentum (SAM and OAM) arise from circular polarization and helical phase structure, respectively [1]. Both are inherently chiral: SAM is defined by the helicity $\sigma = \pm 1$, corresponding to right- and left-handed circular polarization, while OAM is quantified by the integer-valued topological charge $\ell = \pm 1, \pm 2, \dots, \pm \infty$, with the sign indicating handedness and the magnitude the number of phase twists. Together, SAM and OAM form the total angular momentum of light, a central concept in modern photonics that underpin a wide range of applications [2, 3], including classical and quantum communication [4, 5], light-matter interaction [6–8], and optical manipulation [9, 10]. Moreover, these degrees of freedom lie at the heart of structured light [11, 12], i.e., custom-shaped light fields, that fuel a host of exotic phenomena ranging from the emergence of field textures that mimic particle-like topologies across quantum and classical domains, to exotic Berry-phase-driven effects that are enabled by spin-orbit interactions (SOI) [13–15].

Traditionally, SOI in optical systems have been realized through structured light–matter interactions. These include anisotropic media such as patterned liquid crystals that exploit geometric phase [16], metasurfaces that impose spatially varying polarization responses [12, 17–19], or spin-dependent surface waves in dielectric and plasmonic interfaces [20–22]. In tightly focused beams, SOI can emerge as spin-to-orbit conversion in scalar beams [13, 23] or give rise to phenomena such as the orbit-induced spin Hall effects of light [24–26], where cir-

cular polarization components of vectorial fields can separate radially, occupying specific regions in the transverse plane of an optical field. However, to enhance the typically subwavelength and inherently weak SOI phenomena, one generally relies on non-paraxial conditions or tailored materials. This is primarily because these phenomena are significantly suppressed in the paraxial regime due to their minimal magnitude.

Here, we demonstrate a previously unexplored mechanism for SOI effects that exploits the intrinsic topology of vectorial beams, allowing the effect to emerge during free-space paraxial propagation. Specifically, we observe local spin and optical chirality generated solely through paraxial propagation. These quantities play central roles in light-matter interactions: spin governs polarization-dependent selection rules and drives optical torque, while optical chirality underlies linear optical activity such as circular dichroism. We achieve their local generation by engineering the Pancharatnam topological (PT) index ℓ_p of a vector vortex beam, which quantifies the topological winding of its polarization state and, in such beams, determines the net orbital angular momentum [27]. The effect arises from purely topological and propagation-induced processes: differential Gouy phase accumulation between orthogonal polarization components and radial divergence governed by the beam envelope. These results overturn the long-standing assumption that SOI effects require non-paraxial regimes or light-matter interactions, showing instead that the intrinsic topology of structured light alone can produce observable spin-orbit effects. This provides a tunable, material-independent platform for applications in chiral sensing, optical manipulation, and high-dimensional quantum and classical information encoding.

* isaac.nape@wits.ac.za

† K.Forbes@uea.ac.uk

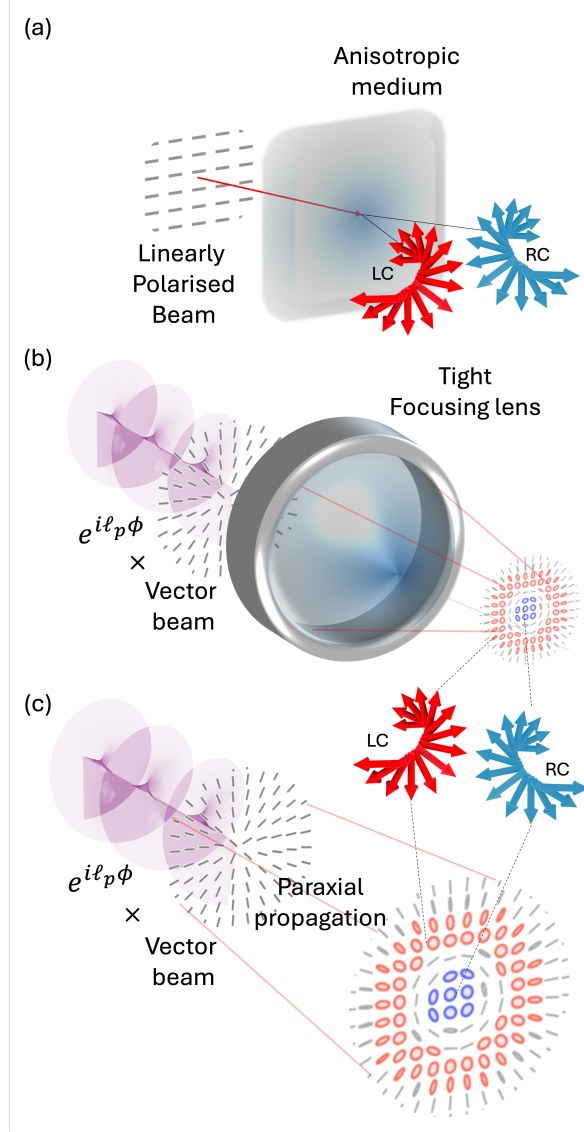


FIG. 1. Concept of spin-separation in vectorial fields. (a) Spin-dependent separation resulting from a vectorial field interacting with an anisotropic medium, therefore resulting in a photonic spin-Hall effect. Lateral transverse shifts are observed depending on the spin components of the incident field. (b) Spin separation induced by tight focusing of a radially polarized vectorial beam carrying a PT phase with a corresponding topological charge, ℓ_p , and (c) reproduced by propagating the same field but through freespace without any interactions with matter. In each case, spin separation is observed in the evolved vector beam, showing regions dominated by right-handed and left-handed circular polarizations.

II. RESULTS

Concept of spin-orbit interactions driven by beam topology. Before demonstrating how topological structuring enables SOI in paraxial light, we briefly outline their origins in light-matter interaction. Optical SOI manifest when initially linearly polarized beams

develop spatially varying spin, typically via interaction with dielectric surfaces, anisotropic and inhomogeneous media, or tight focusing. These processes produce spin-dependent beam shifts such as the Goos-Hänchen and Imbert-Fedorov effects [28, 29], and radial spin separation driven by orbital structure [26], all arising from spin-orbit coupling [13], as illustrated in Fig. 1(a), (b), respectively.

Accordingly, these effects can also be viewed as being produced by polarization-dependent field gradients that separate spin components, akin to spin transport in electronic systems where electron spin-dependent flow and separation in the presence of an electric current can be observed [14]. As the spins separates spatially, two signatures emerge: (i) chiral spin textures with localized optical chirality (helicity), and (ii) spin currents characteristic of photonic spin-Hall effects. Here we show that by encoding topological structure into vector beams, these features can be realized in free-space within the paraxial regime – enabling spin separation and chiral spin flows without relying on strong focusing or complex media.

Topology-driven spin-orbit interactions in paraxial light. To generate SOIs that result in spin generation and separation within laser beams, one can tightly focus (see Fig. 1 (b)) a scalar beam [30–32] or vector vortex beam [25, 26, 33–42] to produce so-called orbit-induced local spin (OILS). However, as we will demonstrate, these effects can also be realized in the paraxial regime, without the need for tight focusing. The approach begins with an optical field that exhibits a spatially varying linear polarization combined with a global azimuthal phase profile, as illustrated (c). The corresponding electric field has the initial profile

$$\mathbf{U}_{\text{in}}(\mathbf{r}) \propto e^{i\ell_p\phi} \times \underbrace{f_{\text{in}}(\mathbf{r}) (e^{i\Delta\ell\phi} \hat{\sigma}_+ + e^{-i\Delta\ell\phi} \hat{\sigma}_-)}_{\text{radial field}}, \quad (1)$$

in polar coordinates, $\mathbf{r} = (r, \phi)$ with σ_{\pm} representing the right and left CP, each marked with azimuthal phase profiles, $\exp(\pm i\Delta\ell\phi)$ with $\Delta\ell \in \mathbb{Z}$. At this point, it is crucial to notice that the polarization components each have the same radial amplitudes ($f_{\text{in}}(\cdot)$). The global phase, which has been factorized from the state, $\exp(i\ell_p\phi)$ characterized by the PT index $\ell_p \in \mathbb{Z}$, encodes the elusive topological features that we are interested in as this controls the spin-orbit interactions in the field. Given the above electric field, the topological phase can be computed from (See Supplementary Material)

$$\phi_p = \arg(\langle \mathbf{U}_{\text{in}}(0) | \mathbf{U}_{\text{in}}(\phi) \rangle) = \frac{\ell_p}{2}\phi, \quad (2)$$

which is directly linked to the PT winding number that is also associated with the total OAM of the VVB (see Supplementary Material). Setting $\ell_p = 0$ produces a typical radially polarized field that does not carry this phase (nor total OAM) and remains unchanged, i.e., maintaining the same polarization profile on propagation. However, for $|\ell_p| > 1$ the fields carries nonzero OAM while the

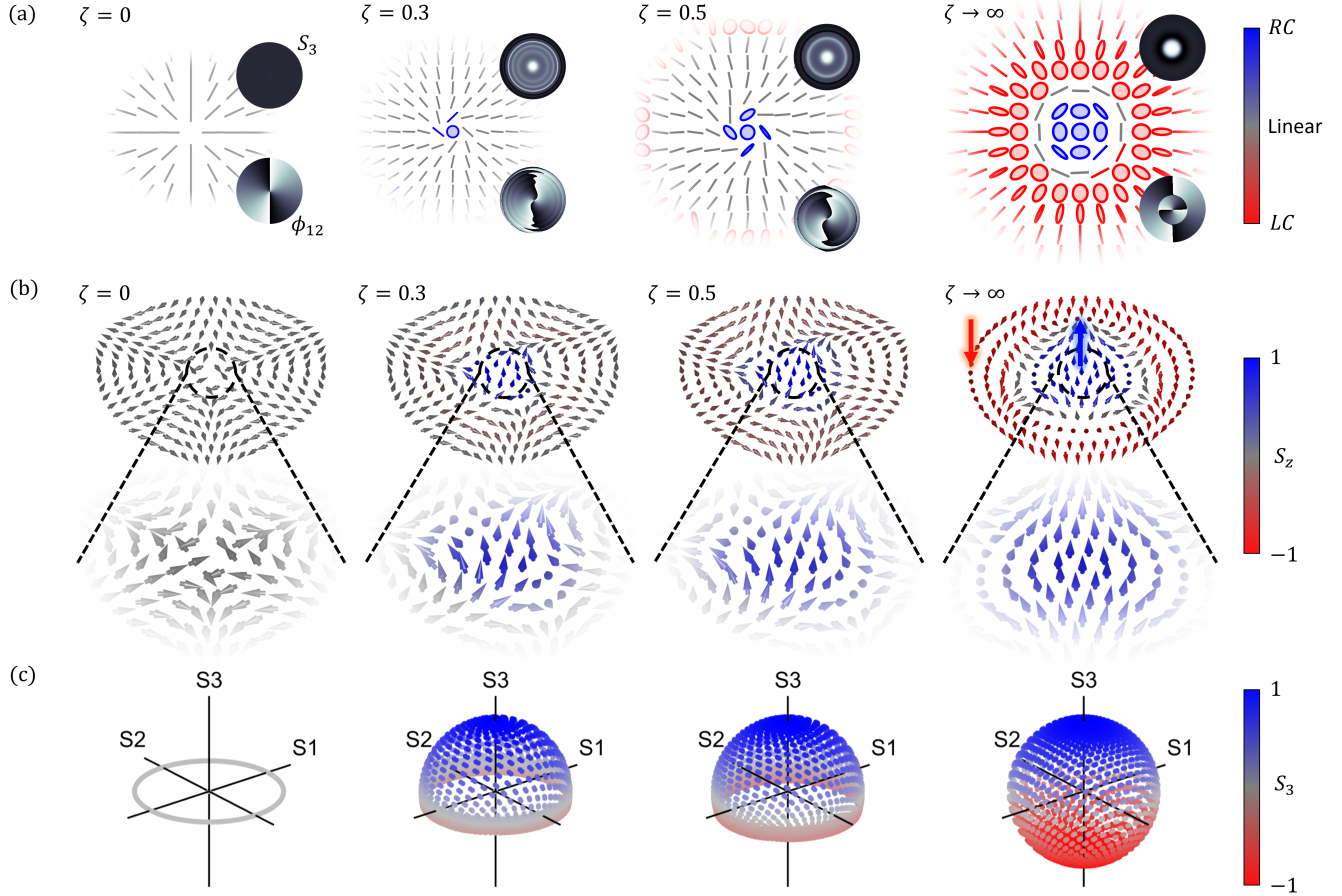


FIG. 2. Revealing the origin of orbit-dependent spin dynamics in paraxial light. (a) A horizontally polarized LG mode (with $\ell_p = 1$ and $p = 0$) incident on a q -plate, produces a vector mode with a radially polarized field pattern (in the near field) but carrying a net OAM charge of ℓ_p . Initially, the field contains zero spin density as it is populated by linear polarization states. On propagation, the beam shows a varying chirality and spin density (S_3), shown via the polarization ellipses, at various propagation planes. These propagation planes are marked by the ratio $\zeta = z/z_R$, with $\zeta = 0$ corresponding to the image plane. The spin density (S_3 , top panel) and the relative phase (ϕ_{12} , bottom inset) are shown at each propagation plane. (b) Spin textured fields represented by spin unit vectors for the various corresponding propagation planes, with selected zoomed-in regions. Initially, the spin vectors point in the transverse plane, then gradually accumulate upward right-circular (RC) and downward left-circular (LC) spin components at the center and away from the origin, respectively. In the far field, there is a clear boundary that separates the LC and RC spin components, indicative of the Hall effect - orbit dependent spin separation. (c) The population of polarization states is shown at each plane on the Poincaré sphere. Initially, only the equator is covered at the waist plane, since the field contains only linear polarization states. Eventually, full coverage is shown, illustrating that the field evolves into a full Poincaré beam.

PT phase causes the polarisation field to change across the beam in the transverse plane on propagation, so that the new field maps as

$$\mathbf{U}_{\text{in}} \rightarrow \mathbf{U} = f_{\ell_A}(\mathbf{r})e^{i\ell_A\phi}\hat{\sigma}_+ + f_{\ell_B}(\mathbf{r})e^{i\ell_B\phi}\hat{\sigma}_-, \quad (3)$$

where $f_{\ell_{A(B)}}(\mathbf{r})$ represent the new field amplitude distributions for each spin component, that now depend on the PT charge, $\ell_{A(B)} = \ell_p \pm \Delta\ell$, respectively. As a consequence, one observes that the spin components separate radially in the field. For example, in the output profile of the concept illustration in Fig. 1 (c), we see that close to the core ($r \approx 0$), the field is dominated by right circular spins and subsequently dominated by left circular

spins as one scans the field radially outward - a key signature of local spin generation - whereas initially the field had no local spin components. This can be measured by quantifying the local optical chirality density and longitudinal spin densities, which are both proportional to the third Stokes parameter (See Supplementary Material for the derivation), S_3 [36], i.e,

$$S_3 = |f_{\ell_A}(r, z)|^2 - |f_{\ell_B}(r, z)|^2, \quad (4)$$

that can be extracted from the transverse plane for various longitudinal coordinates, z . The third Stokes parameter can be measured experimentally via the difference in intensities between the space-dependent ampli-

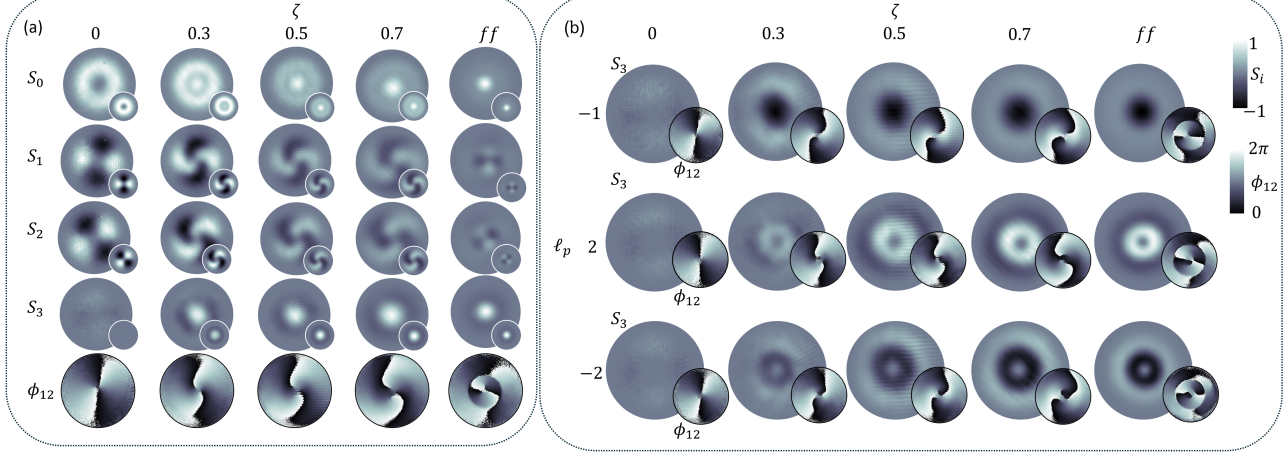


FIG. 3. Experimental stokes parameter analysis. (a) Measured Stokes parameters, S_j , for $\ell_p = 1$ at various propagation planes, labeled here as the ratio $\zeta = z/z_R$ with $\zeta = 0$ corresponding to the image plane. The last row shows the relative phases, ϕ_{12} , showing a winding number $2\Delta\ell \approx 2$ for all propagation planes. (b) The measured z component of the Stokes parameter $S_3(\mathbf{r})$, characterizing the spin density of the field at different planes, ζ and the corresponding relative phase (ϕ_{12} , see inset). This is shown for $\ell_p = -1, 2$ and -2 .

tudes marking each spin state. The reason for extracting the optical chirality C and spin density \mathbf{s} from the stokes parameter (S_3) follows from the fact that in the paraxial regime, these quantities take familiar forms, with the spin being purely longitudinal; $s_z \propto C \propto \sigma I$, where σ is the helicity (for circular polarization $\sigma = \pm 1$, for elliptical $|\sigma| < 1$, and for linear or unpolarized light $\sigma = 0$), and I is the beam intensity. We show that radial spin separation originates from amplitude symmetry breaking due to topological encoding, and elucidate its propagation dependence via S_3 and the associated polarization profiles.

Inducing SOI in paraxial fields through topology-driven amplitude change in propagation. Now we uncover the mechanism that enables one to observe SOI in paraxial beams. Firstly, notice that the vector beams described by Eq. 3 are hybrid-order Poincaré beams (HyOPs) and are not eigenmodes of free-space propagation [43] when $|\ell_p| > 0$. As they propagate, the local states of polarization evolve along z due to differential Gouy phase shifts and radial amplitude variations between the constituent modes that mark the right and left CP states. This leads to a spin-dependent splitting into concentric rings, each carrying opposite circular polarization and different OAM – a signature of propagation-driven optical Hall effect.

To demonstrate this in the paraxial regime, we prepared a scalar horizontally polarized Laguerre-Gaussian (LG) mode, as shown on the left of the concept image in Fig. 1 (c), having a characteristic field profile that can be expressed as

$$LG_{\ell_p}(\mathbf{r})\hat{\mathbf{x}} = f_{\ell_p}(r, z)e^{i\ell_p\phi}\hat{\mathbf{x}}, \quad (5)$$

where $(\hat{\mathbf{x}} = \hat{\sigma}_+ + \hat{\sigma}_-)/\sqrt{2}$ and $\mathbf{r} = (r, \phi, z)$ are the polar coordinates. The LG modes used here have a characteristic radial profile, $f_{\ell_p}(r, z) \propto (\sqrt{2}r/w)^{|\ell_p|} \exp(i(\psi_G + kz) - r^2/w^2)$ where $w[z]$ is the waist size of the embedded Gaussian component of the field (e^{-r^2/w^2}); a Gouy phase $\psi_G = (|\ell_p| + 1)\arctan(z/z_R)$; and an azimuthal phase, $\exp(i\ell_p\phi)$. Note how the topological charge determines the change in the Gouy phase term, as well as the divergence through the radial term. The resulting field will be modulated with a spin-orbit coupling (SOC) device, e.g., a q -plate, at the $z = 0$ plane, yielding the mapping

$$\begin{aligned} LG_{\ell_p}\hat{\mathbf{x}} &\xrightarrow{q\text{-plate}} \mathbf{U}_{in}(\mathbf{r}, z = 0), \\ &= f_{\ell_p}(r) (e^{i\ell_A\phi}\hat{\sigma}_+ + e^{i\ell_B\phi}\hat{\sigma}_-), \end{aligned} \quad (6)$$

therefore producing the HyOP in Eq. (1) but at the $z = 0$ plane, with $\ell_A = \ell_p + \Delta\ell$ and $\ell_B = \ell_p - \Delta\ell$ while $|\Delta\ell|$ is the magnitude of the topological charge transferred by the q -plate for each spin component, i.e. $\pm\Delta\ell$ for σ_{\pm} , respectively. In this work, $\Delta\ell = 1$ due to the q -plate. While the q -plate is employed to generate the radially polarized mode, we emphasize that it is not fundamental to the SOI effect under investigation. It merely serves as a convenient means to prepare the desired beam, and alternative methods could be equally suitable, e.g., using dynamic phase control with spatial light modulators and interferometers.

At this stage, the field in Eq. (6) is a typical vectorial field that is linearly polarized and carries the PT phase, which at $z = 0$, has no impact of the field. One would expect the field to evolve like a cylindrical vortex beam that maintains its polarization profile

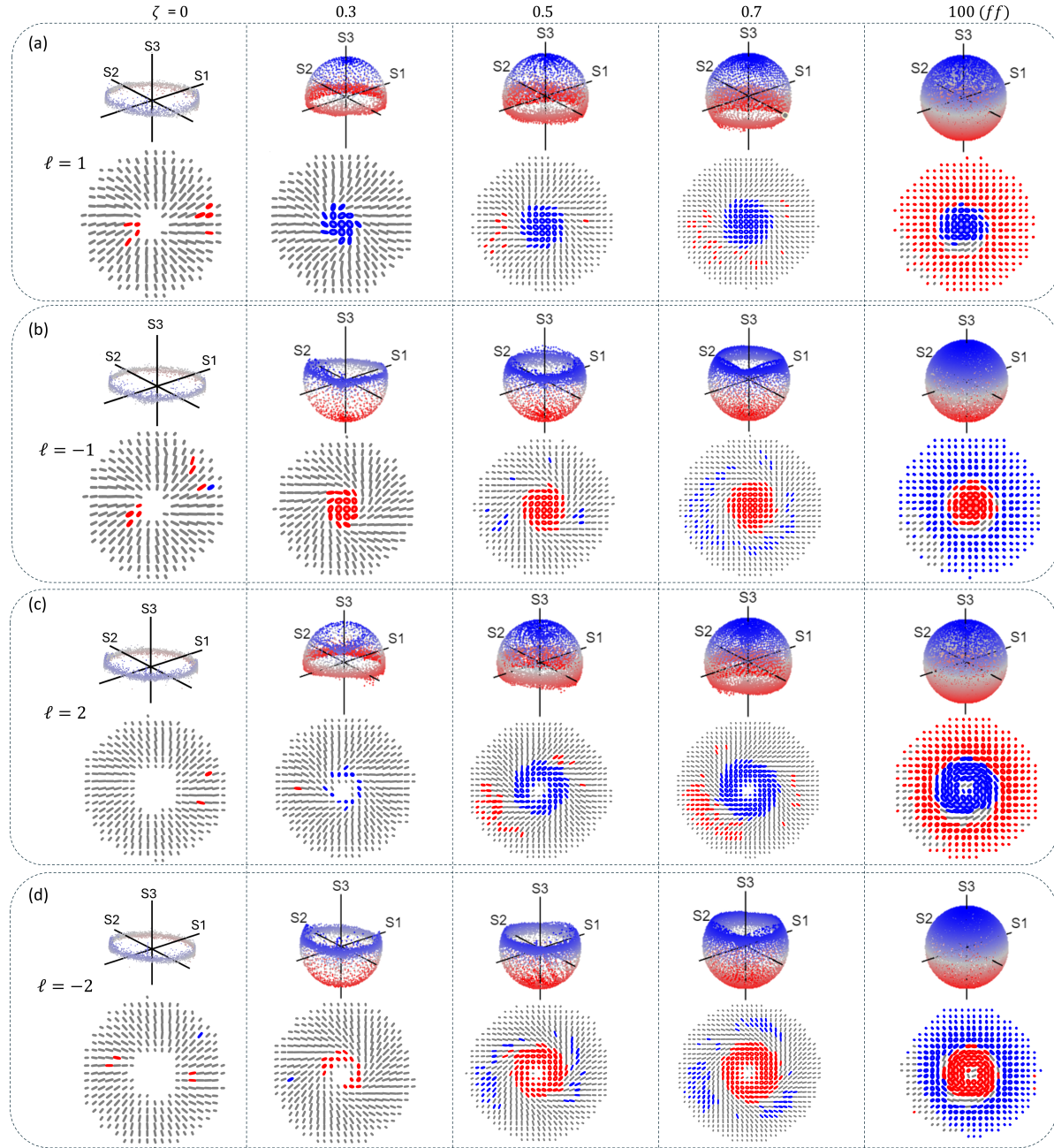


FIG. 4. Observing orbit induced spin induction upon propagation. Reconstructed Poincaré sphere coverage and polarization ellipses for Pancharatnam topological indexes (a) $\ell_p = 1$ and (b) $\ell_p = -1$ at various propagation planes ($\zeta = z/z_R$). The same plots are shown for topological phases (c) $\ell_p = 2$ and (d) $\ell_p = -2$, illustrating the emergence of spin from a vectorial field that initially has zero spin density in the paraxial regime.

upon propagation, however, the global phase, $\exp(i\ell_p\phi)$, carrying the PT phase, causes an asymmetry in the amplitudes. Theoretical simulations of the resulting polarization ellipse profiles are depicted in Fig. 2 (a), illustrating the change in chirality (accumulation of CP components) as the resulting mode propagates. These are obtained using the localized Stokes vector ($\mathbf{S}(\mathbf{r}) = \langle S_1(\mathbf{r}), S_2(\mathbf{r}), S_3(\mathbf{r}) \rangle$) components (See Methods

for Stokes parameter reconstruction procedure). Here, the propagation planes, $\zeta = z/z_R$, are defined relative to the Rayleigh range (z_R). The spin densities (S_3) are shown as the top insets of Fig. 2 (a), confirming the increase in spin density while the relative phase ($\phi_{12} = \arg(S_1(\mathbf{r}) + iS_2(\mathbf{r})) = 2\Delta\ell\phi$, from which the polarization order ($\eta = \Delta\ell/2$) can be determined, is preserved, shown in the bottom insets of Fig. 2 (a).

The spin textures, illustrating the directional spin unit vectors, satisfying $\sqrt{S_1^2(\mathbf{r}) + S_2^2(\mathbf{r}) + S_3^2(\mathbf{r})} = 1$, are shown in Fig. 2 (b). Here we see that initially at the $\zeta = 0$ (equivalently $z = 0$) plane, the third Stokes parameter evaluates to zero at all positions of \mathbf{r} as shown in Fig. 2 (a) which is reflected in Fig. 2 (b) where the spin vectors are all in plane. This is because the spatial amplitudes are the same ($|f_{\ell_A}|^2 = |f_{\ell_B}|^2 = |f_{\ell_p}|^2$) for the spin components. Therefore, the field is not chiral at this specific plane ($z = 0$). However, this is not the case for $\zeta > 0$.

The position-dependent amplitudes have been derived analytically for cases where an LG mode is incident on a phase element that imparts a phase of $e^{\pm i\Delta\ell\phi}$ similar to the phases imparted by the q -plate. It has been shown that the LG mode profile evolves into an elegant Laguerre-Gaussian (eLG) [44] mode or, equivalently, into a Hypergeometric Gaussian (HGG) mode [45]. In this article, we will use eLGs to represent the modes as they evolve, i.e. $eLG_{p_{A(B)}}^{\ell_{A(B)}}$, with a topological charge of $\ell_{A(B)} = \ell_p \pm \Delta\ell$ and a radial index $p_{A(B)} = \frac{1}{2}(|\ell_p| - |\ell_{A(B)}|)$ [44]. These quantum numbers explicitly depend on the Pancharatnam index, ℓ_p . Therefore, the amplitude changes in the polarization components of the fields satisfying $f_{\ell_{A(B)}}(r, z) \equiv |eLG_{p_{A(B)}}^{\ell_{A(B)}}(r, z)|$, are responsible for the observed polarization profile changes that in turn produce areas of chirality and longitudinal spin (i.e.: $S_3 \neq 0$) in the propagated fields. The angular spectrum (equivalently the farfield amplitude profile) of these modes has the form (see Supplementary Material for complete expression),

$$\begin{aligned} eLG_{p_{A(B)}}^{\ell_{A(B)}}(\rho, z \rightarrow \infty) &\propto i^{-\ell_{A(B)}} \rho^{|\ell_{A(B)}|} L_{p_{A(B)}}^{|\ell_{A(B)}|} [\rho^2] \\ &\times \exp(i\ell_{A(B)}\phi), \end{aligned} \quad (7)$$

where ρ is the normalized radial (wavenumber) coordinate showing the explicit dependence on the radial term $\rho^{|\ell_{A(B)}|} = \rho^{|\ell_p \pm \Delta\ell|}$ which controls the radial distribution of the modes (see Supplementary Material for more details about radial amplitude separation). Therefore, this radial factor is the source of the asymmetry in the spin components that can be observed in the transverse plane of the fields. In Fig. 2 (c) we map the fields onto the Poincaré sphere and show the population of polarization states across a field. Initially, the field at $z = 0$, maps onto a ring on the equator of the sphere because the field has no longitudinal spin components ($S_3 = 0$). However, as the field propagates, gradual coverage over the sphere is achieved, indicating the emergence of a longitudinal spin component ($S_3 > 0$) in the fields. Furthermore, because states near the origin have a higher intensity, only one half of the Poincaré sphere is covered first and other states are gradually populated as the beam propagates. Eventually, the farfield ($z \rightarrow \infty$) is fully occupied by all possible spin states. This is observed taking into account that the intensity of the fields in the radial direction decreases,

and nearly about 8% of the peak intensity is detected with a typical off-the-shelf CCD camera under the influence of stray light and shot noise in the detector (CCD). In the Supplementary Material, we show the case where the entire field intensity can be resolved completely, and find that full coverage is observed immediately upon propagation; however, we use the former to mirror experimental conditions.

Experimental Validation Next, we performed an experiment to validate the above (See experimental details in Methods). Horizontally polarized LG modes were prepared sequentially (using a spatial light modulator) with varying topological charges, $\ell_p \in \{1, -1, 2, -2\}$, with each mode imaged onto a q -plate that transfers a net charge of $\pm\Delta\ell = \pm 1$ for each circular polarization component σ_{\pm} , respectively. This produces our HyOP mode, carrying a Pancharatnam topological charge ℓ_p . The Stokes parameters are shown in Fig. 3 (a) at various propagation planes ($\zeta = \{0, 0.3, 0.5, 0.7, \text{farfield } (ff)\}$) first for $\ell_p = 1$, with the last row showing the relative phase ϕ_{12} . Although the S_1 and S_2 Stokes parameters have the same number of lobes as shown in the two middle columns (second and third rows) of Fig. 3 (a), the only change observed is in the spiralling nature of the pattern upon propagation due to curvature and relative Gouy phase between the evolving field's components. The twist of the spiral phase observed in the relative phase (ϕ_{12} , last row of Fig. 3 (a)) is seen to depend on the sign of the Pancharatnam topological charge during propagation. However, its handedness (direction of increasing phase in the azimuth direction) is preserved. On the other hand, the total beam intensity (S_0) and spin densities (S_3) are seen to change upon propagation as predicted, due to the amplitude change, with the left-handed CP component occupying the centre. In contrast, the right-handed CP components dominate regions further away from the centre. Next, in Fig. 3 (b) we varied the input Pancharatnam topological charge ($\ell_p \in \{-1, 2, -2\}$) and show the spin densities (S_3) and the relative phases ϕ_{12} . All the cases also exhibit identical relative phase profiles, although the spin densities (S_3) differ, resulting in different amplitude responses. In contrast to $\ell_p = 1$, $\ell_p = -1$, it produces a spin density profile, S_3 , that is inverted, showing that the chirality in the field has switched; now the right-handed CP amplitudes dominate in the center, whereas the left-handed CP components dominate at a distance away from the centre. For $\ell_p = \pm 2$ we also see the same trend where the dominant polarization switches depending on the input topological charge. Further, the magnitude of the input charge (ℓ_p) is seen to control the radial profile of the spin density (S_3) owing to the radial modes that emerge in the field upon propagation, since the field components become eLG modes that have regions of nonoverlapping intensities. Moreover, for $\ell_p = \pm 2$, a vortex is observed since both circular polarization components have non-zero OAM after passing through the q -plate, which can

also be inferred from the S_3 components. We emphasise that the same q -plate was used to obtain these results, indicating that the local chirality is primarily attributed to the presence of Pancharatnam topological charge in the fields. The sphere coverage and polarization (ellipse) profiles at different propagation planes are depicted in Fig. 4. The polarization ellipses are represented in terms of handedness, with red indicating left-handed CP and blue representing right-handed CP.

Results were obtained for positive topological charge $\ell_p > 0$ (middle and bottom rows of Fig. 4), resulting in right-handed CP at the origin of the field. Conversely, for $\ell_p < 0$ (top row of Fig. 4), left-handed CP was observed at the center/origin of the field. We observe that the fields only contain linearly polarized states at the plane of the q -plate, as expected, since only linear polarizations are observed, indicated by the population of the fields on the equator of the Poincaré sphere. This can be inferred from the radially oriented linear polarization states, indicating that $S_3 \approx 0$. The presence of a few observed ellipses at this plane can be attributed to experimental errors induced by the waveplates. This can be improved through careful calibration of the waveplates. As we observe propagation, circular polarizations begin to form, indicating an increase in the spin density of the field. For $\ell_p = 1(-1)$, the accumulation of elliptical polarization states is also seen through the occupation of states beyond the equator. In fact, the polarization states initially dominate the top half of the sphere, since the LC (RC) components have a larger amplitude contribution and eventually cover the whole sphere once the beam approaches the farfield. Similarly, this is observed for $\ell_p = \pm 2$, however, the structure has a characteristic vortex at the centre.

Topology-driven optical Hall effect.

Lastly, in Fig. 5, we show the measured farfield spin textures for each of the HyOP modes having different Pancharatnam topological charges. In these illustrations, it can be seen that for $\ell_p = 0$ all the spin vectors lie in the transverse plane, showing that there is no spin separation. However, once $\ell_p > 0$, the separation of RC and LC components is observed, confirming the topologically driven nature of the spin separation in the optical field, which only depends on ℓ_p . Therefore, the initial Pancharatnam topological charge, which characterizes the net OAM of the modes, induces transverse spin currents analogous to an electric field that induces similar currents in a magnetic system. The spin currents can be measured from $\bar{J} = \langle \frac{\partial S_3}{\partial y}, -\frac{\partial S_3}{\partial x} \rangle$. We show this for our experimental results in the insert of Fig. 5, demonstrating an azimuthal spin current in each case. This is because of the radial spin gradient seen in the S_3 components of the field with an abrupt switch in helicity observed in each case. In fact, more generally, this Hall effect can be interpreted as a spin-orbit Hall effect arising from the spatial separation of spin and orbital angular momentum components in vector vortex beams during propagation. For example, the inner and outer rings of Fig. 4 (c) in the

ff possess an azimuthal phase of $\exp(i\phi)$ and $\exp(i3\phi)$, respectively. Although we have not directly measured the OAM content of each polarization component, the fact that their regions do not overlap suggests that each mode may contribute an OAM density confined to its respective nonoverlapping area. Finally, it is important to emphasise that spin and optical chirality in these beams are local properties. Due to the divergence of the full three-dimensional integrals, the (integral) total values of the spin and optical chirality for beams are instead expressed in terms of their linear densities, i.e., the corresponding quantities per unit length along the z -axis: $\propto \int S_3 d\mathbf{r}_\perp = 0$. Clearly upon free-space propagation of the radially polarized field the integral values are conserved.

III. DISCUSSION

The emergence of non-zero spin and optical chirality densities (quantified by S_3) from an initially spin- and chirality-free beam exemplifies orbit-induced local spin – OILS. While OILS has traditionally been linked to scalar [30–32] and vector vortex beams [25, 26, 33–42] in the non-paraxial regime, our findings show that, for vector vortex beams, OILS can also occur in the paraxial regime via a topologically driven optical Hall effect of light [13], which was previously believed to require tight focusing. For instance, in a recent experiment of Wu *et al.* [26], a linearly polarized Gaussian beam is first modulated using a spatial light modulator to produce a linearly polarized vortex beam. This was then passed through an S -plate to generate radially polarized light, which is subsequently tightly focused. However, the spatial separation of S_3 components observed in their experiment can be attributed to the focusing-independent, topologically driven mechanism we describe. While tight focusing may be necessary to produce measurable mechanical effects, such as particle manipulation, it is not the fundamental origin of OILS in vector vortex beams. Instead, we demonstrate that the underlying effect is paraxial and arises from the optical Hall effect of structured light.

We have shown that the Pancharatnam topological charge ℓ_p is responsible for inducing optical chirality and spin angular momentum in the paraxial regime. To demonstrate this, we employed a radially polarized beam with non-zero net OAM and a polarization order of $\eta = 1$. Although the polarization order remains invariant during propagation, the amplitude distribution of this mode evolves, giving rise to spin and chirality, as visualized through the Stokes parameter S_3 . By varying the Pancharatnam topological charge ℓ_p , via an optical Hall effect of paraxial light, we demonstrate control over the resulting optical spin and chirality densities. We emphasize that the SOC device sets the OAM difference $\ell_A - \ell_B = 2\Delta\ell$ (and equivalently the mode order, η) between the two spin components which drove the separation between the RCP and LCP components upon

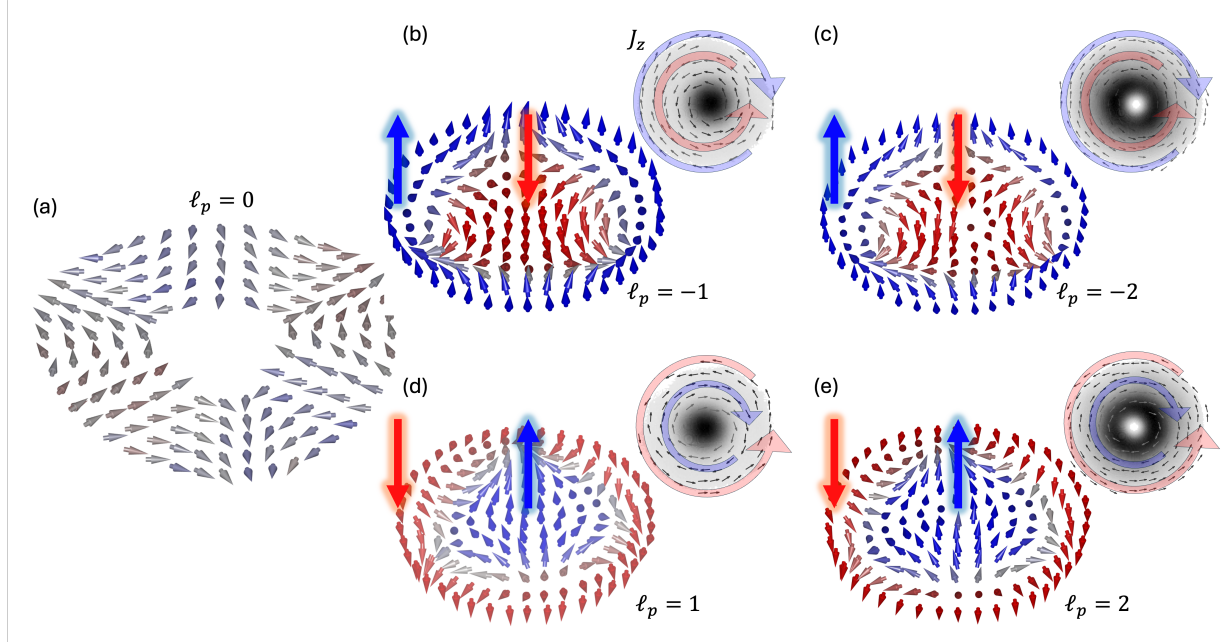


FIG. 5. Emergent orbit-induced Hall effect. Experimental spin textures for the farfield modes given the Pancharatnam topological charge, ℓ_p , of (a) 0, (b) -1, (c) -2, (d) 1 and (e) 2, illustrating an orbit-induced Hall effect. The transverse spin separation is visualized by the spin-current insets, which reveal an azimuthal flow that reverses direction as it approaches the field's origin. This behaviour shows that the polarization handedness is well-defined near the center and changes beyond a certain radial distance, indicative of an optical spin-Hall effect. The insets show the spin currents (\bar{J}) which reveal the azimuthal spin currents due to the spin-Hall effect.

propagation. Choosing an SOC device with a larger $\Delta\ell$ (and $\ell_p \neq 0$) leads to a more pronounced Hall effect. This is due to the fact that the ring size of these modes behave roughly according to $r^{|\ell_p \pm \Delta\ell|}$, which means that the greater the difference between the magnitude of the OAM values for each polarization component, the larger their radial separation in the far-field. While we employed an SOC device for its convenience in generating such beams, the underlying SOI effect is not unique to this method and can also be realized using alternative beam-shaping approaches such as spatial light modulators or interferometric schemes.

IV. CONCLUSION

This work reveals a previously underexplored mechanism for SOI interactions that generate local spin and chirality in paraxial structured light, governed by the Pancharatnam topological charge ℓ_p . These insights not only deepen our understanding of spin-orbit interactions in light but also open new avenues for optical control in applications ranging from chiral spectroscopy and nano-manipulation to robust spin-based photonic devices for quantum information technologies.

V. METHODS

A. Experimental

We validated our theoretical prediction that the Pancharatnam topological charge gives rise to chirality on the propagation of the optical field through the experimental setup shown in Fig. 6. The experimental setup consisted of three parts, namely: (1) the generation, (2) propagation and (3) detection (via Stokes polarimetry). In the generation stage, a horizontally polarized Gaussian beam from a HeNe-663 nm laser was expanded and collimated to illuminate a reflective HOLOEYE PLUTO-2.1 LCOS SLM. This scalar Gaussian mode was structured using a LG complex-amplitude hologram with topological charge of $\ell_p \in \{1, -1, 2, -2\}$ encoded on the SLM [top left corner of Fig. 6 (a)], thus producing a LG mode with a phase of $e^{i\ell_p\phi}$. A 4f-imaging system consisting of lenses $F_1, F_2 = 300$ mm was used to image the plane of the SLM onto a q -plate. Since the SLM produces multiple diffraction orders, a spatial filter or aperture (AP) was placed in the focal plane of F_1 to select only the positive first order and filter out the remaining orders. The selected first order LG scalar mode was then imaged onto the focal plane of F_2 where the q -plate was located. The q -plate is capable of generating a vector vortex beam by introducing a geometric phase through the variation of the input beam's polarization, which then imparts OAM. The q -plate (in

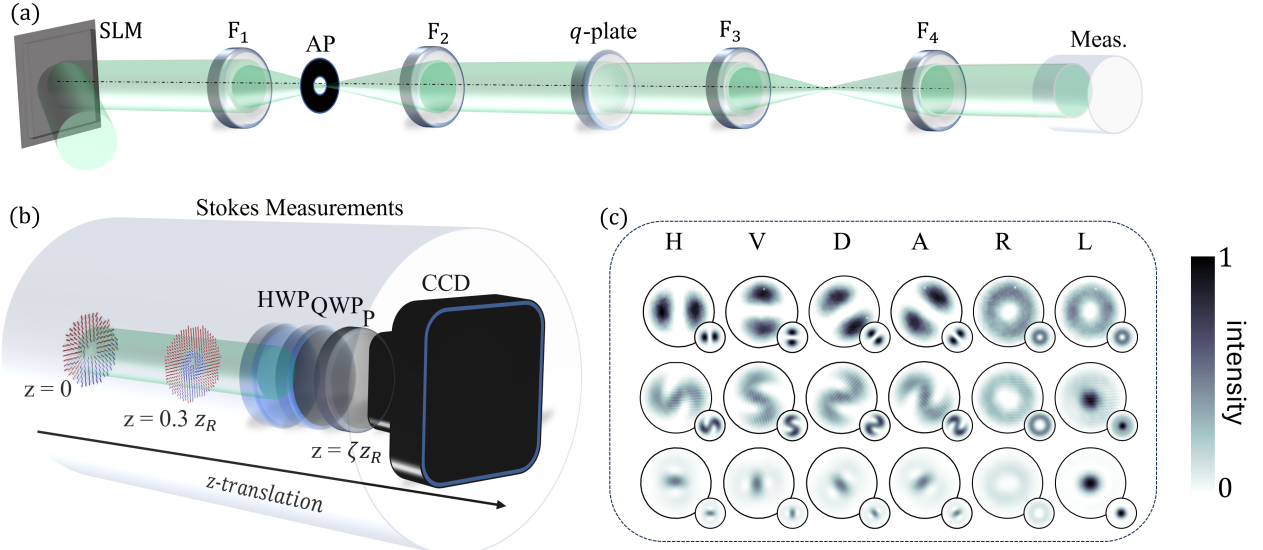


FIG. 6. **Experimental Setup:** Schematic of the experimental setup depicting (a) the generation and (b) detection components. SLM: spatial light modulator, AP: aperture, HWP: half-wave plate, QWP: quarter-wave plate, P: polarizer, CCD: charged coupled device. (c) Experimentally recorded polarization intensities for H , V , D , A , R and L for 3 separate propagation planes (inserts denote corresponding theoretical intensity profiles). $\zeta = 0, 0.5$ and the farfield.

our case having $q = \frac{1}{2}$) converted the incoming horizontally polarized scalar mode into a radially polarized vector mode. Here the horizontally polarized light ($|H\rangle$) can be written as a superposition of right- and left-handed CP, ($|R\rangle$ and $|L\rangle$, respectively) with the q -plate converting $|L\rangle$ into $|R\rangle$ and vice-versa, while introducing a phase of $e^{i(\ell-2q)\phi}$ and $e^{i(\ell+2q)\phi}$ to $|R\rangle$ and $|L\rangle$, respectively. A second 4f-imaging system, comprising of lenses F_3 , $F_4 = 100$ mm, imaged the plane of the q -plate to the focal plane of lens F_4 . Between lens F_4 and the charge-coupled device (CCD), we performed Stokes measurements which are further explained below. The CCD was propagated across six different Rayleigh ranges (z_R) with the Stokes measurements performed at each individual plane. The components for the Stokes measurements are shown in Fig. 6 (b), with example polarization intensities for 3 separate propagation planes shown in each row of Fig. 6 (c).

B. Stokes parameters and measurements

The components of the locally normalized Stokes vector can then be expressed as

$$\mathbf{S}(\mathbf{r}) = \begin{pmatrix} \cos(\Phi) \sin(\beta) \\ \sin(\Phi) \sin(\beta) \\ \cos(\beta) \end{pmatrix}, \quad (8)$$

where Φ and β are the azimuthal and zenith coordinates on the Poincaré sphere.

Here, we will give an overview of the representation of the Stokes parameters and the measurement approach used. The reader is advised to view other sources of Stokes polarimetry literature for more detailed and in-depth explanations [46]. The four Stokes parameters can be written in terms of the six polarization intensities, namely I_H, I_V, I_D, I_A, I_R and I_L , as follows [47]:

$$S_0 = I_R + I_L, \quad (9)$$

$$S_1 = I_H - I_V, \quad (10)$$

$$S_2 = I_D - I_A, \quad (11)$$

$$S_3 = I_R - I_L. \quad (12)$$

H, V, D, A, R and L denote horizontal, vertical, diagonal (45°), anti-diagonal (135°), right- and left-handed CP, respectively. Three optical elements, namely a polarizer and two retarders (in the form of a half-wave plate (HWP) and quarter-wave plate (QWP)) can be used to measure the above-mentioned six intensity measurements [as shown in Fig. 6 (b)]. The four linear polarization intensities (I_H, I_V, I_D and I_A) can be measured with a polarizer (for I_H and I_V) and a HWP and polarizer (for I_D and I_A) as the polarizer's transmission axis transmits the various polarization components in accordance with $I(0^\circ) = I_H$ and $I(90^\circ) = I_V$, while the HWP rotates I_D

to I_H and I_A to I_V . By introducing a QWP, which produces a phase shift of $\frac{\pi}{2}$ between the x and y component of the electric field, one can measure circular intensities (I_R, I_L), as follows: $I(45^\circ, 90^\circ) = I_R, I(135^\circ, 90^\circ) = I_L$. Therefore, by placing a QWP (set at 90°) before a polarizer (set initially at 45° and then 135°) the circular intensities (I_R, I_L) can be measured.

ACKNOWLEDGMENTS

The authors thank Andrew Forbes and Ram Khumar for their insightful discussions. I.N. acknowledges support from the South African Quantum Technology Initiative (SAQuTi). I.N. and A.D. gratefully acknowledge funding from the National Research Foundation (NRF) and the Rental Pool Programme (RPP) of South Africa.

AUTHOR CONTRIBUTIONS

K.A.F. conceived the idea, and I.N. conceived the experiment. I.N and A.D supervised the experiment. L.M. performed the experiment and collected the data, while L.M., together with P.O., carried out the data analysis. All authors contributed to the writing and revisions of the manuscript.

COMPETING INTERESTS

The authors have no conflicts to declare.

-
- [1] Konstantin Y Bliokh and Franco Nori. Transverse and longitudinal angular momenta of light. *Physics Reports*, 592:1–38, 2015.
 - [2] Andrew Forbes, Light Mkhumbuza, and Liang Feng. Orbital angular momentum lasers. *Nature Reviews Physics*, 6(6):352–364, 2024.
 - [3] Sonja Franke-Arnold. 30 years of orbital angular momentum of light. *Nature Reviews Physics*, 4(6):361–361, 2022.
 - [4] Yijie Shen, Xuejiao Wang, Zhenwei Xie, Changjun Min, Xing Fu, Qiang Liu, Mali Gong, and Xiaocong Yuan. Optical vortices 30 years on: Oam manipulation from topological charge to multiple singularities. *Light: Science & Applications*, 8(1):90, 2019.
 - [5] Isaac Nape, Bereneice Sephton, Pedro Ornelas, Chane Moodley, and Andrew Forbes. Quantum structured light in high dimensions. *APL Photonics*, 8(5), 2023.
 - [6] Mohamed Babiker, David L Andrews, and Vassilis E Lembessis. Atoms in complex twisted light. *Journal of Optics*, 21(1):013001, 2019.
 - [7] Guillermo F Quinteiro Rosen, Pablo I Tamborenea, and Tilmann Kuhn. Interplay between optical vortices and condensed matter. *Reviews of Modern Physics*, 94(3):035003, 2022.
 - [8] A Porfirev, S Khonina, and A Kuchmizhak. Light-matter interaction empowered by orbital angular momentum: Control of matter at the micro-and nanoscale. *Progress in Quantum Electronics*, 88:100459, 2023.
 - [9] Miles Padgett and Richard Bowman. Tweezers with a twist. *Nature photonics*, 5(6):343–348, 2011.
 - [10] Yuanjie Yang, Yu-Xuan Ren, Mingzhou Chen, Yoshihiko Arita, and Carmelo Rosales-Guzmán. Optical trapping with structured light: a review. *Advanced Photonics*, 3(3):034001–034001, 2021.
 - [11] Andrew Forbes, Michael de Oliveira, and Mark R Dennis. Structured light. *Nature Photonics*, 15(4):253–262, 2021.
 - [12] Chao He, Yijie Shen, and Andrew Forbes. Towards higher-dimensional structured light. *Light: Science & Applications*, 11(1):205, 2022.
 - [13] Konstantin Yu Bliokh, Francisco J Rodríguez-Fortuño, Franco Nori, and Anatoly V Zayats. Spin-orbit interactions of light. *Nature Photonics*, 9(12):796–808, 2015.
 - [14] Eliahu Cohen, Hugo Larocque, Frédéric Bouchard, Farshad Nejadsattari, Yuval Gefen, and Ebrahim Karimi. Geometric phase from aharonov-bohm to pancharatnam-berry and beyond. *Nature Reviews Physics*, 1(7):437–449, 2019.
 - [15] Yijie Shen, Qiang Zhang, Peng Shi, Luping Du, Xiaocong Yuan, and Anatoly V Zayats. Optical skyrmions and other topological quasiparticles of light. *Nature Photonics*, 18(1):15–25, 2024.
 - [16] Peng Chen, Bing-Yan Wei, Wei Hu, and Yan-Qing Lu. Liquid-crystal-mediated geometric phase: from transmissive to broadband reflective planar optics. *Advanced Materials*, 32(27):1903665, 2020.
 - [17] Patrice Genevet, Federico Capasso, Francesco Aieta, Mohammadreza Khorasaninejad, and Robert Devlin. Recent advances in planar optics: from plasmonic to dielectric metasurfaces. *Optica*, 4(1):139–152, 2017.
 - [18] Ahmed H Dorrah and Federico Capasso. Tunable structured light with flat optics. *Science*, 376(6591):eabi6860, 2022.
 - [19] Arseniy I Kuznetsov, Mark L Brongersma, Jin Yao, Mu Ku Chen, Uriel Levy, Din Ping Tsai, Nikolay I Zheludev, Andrei Faraon, Amir Arbabi, Nanfang Yu, et al. Roadmap for optical metasurfaces. *ACS photonics*, 11(3):816–865, 2024.
 - [20] Konstantin Y Bliokh, Daria Smirnova, and Franco Nori. Quantum spin hall effect of light. *Science*, 348(6242):1448–1451, 2015.
 - [21] Peter Lodahl, Sahand Mahmoodian, Søren Stobbe, Arno Rauschenbeutel, Philipp Schneeweiss, Jürgen Volz, Hannes Pichler, and Peter Zoller. Chiral quantum optics. *Nature*, 541(7638):473–480, 2017.
 - [22] DG Suárez-Forero, M Jalali Mehrabad, C Vega, A González-Tudela, and M Hafezi. Chiral quantum optics: Recent developments and future directions. *PRX Quantum*, 6(2):020101, 2025.
 - [23] Konstantin Y Bliokh, Miguel A Alonso, Elena A Ostrovskaya, and Andrea Aiello. Angular momenta and spin-orbit interaction of nonparaxial light in free space. *Physical Review A*, 82(6):063825, 2010.

- [24] Shenhe Fu, Chaoheng Guo, Guohua Liu, Yongyao Li, Hao Yin, Zhen Li, and Zhenqiang Chen. Spin-orbit optical hall effect. *Physical Review Letters*, 123(24):243904, 2019.
- [25] Hehe Li, Chenghao Ma, Jingge Wang, Miaoqiao Tang, and Xinzhong Li. Spin-orbit hall effect in the tight focusing of a radially polarized vortex beam. *Optics Express*, 29(24):39419–39427, 2021.
- [26] Yi-Jing Wu, Pan-Pan Yu, Yi-Fan Liu, Jing-Han Zhuang, Zi-Qiang Wang, Yin-Mei Li, Cheng-Wei Qiu, and Lei Gong. Controllable microparticle spinning via light without spin angular momentum. *Physical Review Letters*, 132(25):253803, 2024.
- [27] Avi Niv, Gabriel Biener, Vladimir Kleiner, and Erez Hasman. Manipulation of the pancharatnam phase in vectorial vortices. *Optics Express*, 14(10):4208–4220, 2006.
- [28] Konstantin Y Bliokh and Andrea Aiello. Goos–hänchen and imbert–fedorov beam shifts: an overview. *Journal of Optics*, 15(1):014001, 2013.
- [29] Minkyung Kim, Younghwan Yang, Dasol Lee, Yeseul Kim, Hongyoon Kim, and Junsuk Rho. Spin hall effect of light: from fundamentals to recent advancements. *Laser & Photonics Reviews*, 17(1):2200046, 2023.
- [30] Panpan Yu, Qian Zhao, Xinyao Hu, Yinmei Li, and Lei Gong. Orbit-induced localized spin angular momentum in the tight focusing of linearly polarized vortex beams. *Optics Letters*, 43(22):5677–5680, 2018.
- [31] VV Kotlyar, AG Nalimov, AA Kovalev, AP Porfirev, and SS Stafeev. Spin-orbit and orbit-spin conversion in the sharp focus of laser light: Theory and experiment. *Physical Review A*, 102(3):033502, 2020.
- [32] Kayn A Forbes and Garth A Jones. Measures of helicity and chirality of optical vortex beams. *Journal of Optics*, 23(11):115401, 2021.
- [33] Lei Han, Sheng Liu, Peng Li, Yi Zhang, Huachao Cheng, and Jianlin Zhao. Catalystlike effect of orbital angular momentum on the conversion of transverse to three-dimensional spin states within tightly focused radially polarized beams. *Physical Review A*, 97(5):053802, 2018.
- [34] Manman Li, Yanan Cai, Shaohui Yan, Yansheng Liang, Peng Zhang, and Baoli Yao. Orbit-induced localized spin angular momentum in strong focusing of optical vectorial vortex beams. *Physical Review A*, 97(5):053842, 2018.
- [35] Peng Shi, Luping Du, and Xiaocong Yuan. Structured spin angular momentum in highly focused cylindrical vector vortex beams for optical manipulation. *Optics Express*, 26(18):23449–23459, 2018.
- [36] Kayn A Forbes. Spin angular momentum and optical chirality of poincaré vector vortex beams. *Journal of Optics*, 26(12):125401, 2024.
- [37] Peiwen Meng, Zhongsheng Man, AP Konijnenberg, and HP Urbach. Angular momentum properties of hybrid cylindrical vector vortex beams in tightly focused optical systems. *Optics Express*, 27(24):35336–35348, 2019.
- [38] Tao Geng, MIN Li, and Hanming Guo. Orbit-induced localized spin angular momentum of vector circular airy vortex beam in the paraxial regime. *Optics Express*, 29(9):14069–14077, 2021.
- [39] Yiqi Fang, Meng Han, Peipei Ge, Zhenning Guo, Xiaoyang Yu, Yongkai Deng, Chengyin Wu, Qihuang Gong, and Yunquan Liu. Photoelectronic mapping of the spin-orbit interaction of intense light fields. *Nature Photonics*, 15(2):115–120, 2021.
- [40] Yanxiang Zhang, Zijing Zhang, Yuan Zhao, and Zhongquan Nie. Ultrafast spin-to-orbit and orbit-to-local-spin conversions of tightly focused hybirdly polarized light pulses. *Advanced Photonics Research*, 3(3):2100308, 2022.
- [41] Zhongsheng Man, Yuquan Zhang, and Shenggui Fu. Polarization singularities hidden in a deep subwavelength confined electromagnetic field with angular momentum. *Optics Express*, 30(17):31298–31309, 2022.
- [42] Fengqi Liu, Jingqi Song, Naichen Zhang, Xiangyu Tong, Mingli Sun, Bingsong Cao, Kaikai Huang, Xian Zhang, and Xuanhui Lu. Manipulation of optical orbit-induced localized spin angular momentum using the periodic edge dislocation. *Optics Express*, 32(6):9867–9876, 2024.
- [43] María M Sánchez-López, Jeffrey A Davis, Ignacio Moreno, Aarón Cofré, and Don M Cottrell. Gouy phase effects on propagation of pure and hybrid vector beams. *Optics Express*, 27(3):2374–2386, 2019.
- [44] Vasilios Cocotos, Light Mkhumbuza, Kayn A Forbes, Robert de Mello Koch, Angela Dudley, and Isaac Nape. Laguerre–gaussian modes become elegant after an azimuthal phase modulation. *Optics Letters*, 50(6):1913–1916, 2025.
- [45] Ebrahim Karimi, Gianluigi Zito, Bruno Piccirillo, Lorenzo Marrucci, and Enrico Santamato. Hypergeometric-gaussian modes. *Optics letters*, 32(21):3053–3055, 2007.
- [46] Keshaan Singh, Najmeh Tabebordbar, Andrew Forbes, and Angela Dudley. Digital stokes polarimetry and its application to structured light: tutorial. *JOSA A*, 37(11):C33–C44, 2020.
- [47] Dennis H Goldstein. Polarization measurements. In *Encyclopedia of Optical and Photonic Engineering (Print-Five Volume Set)*, pages 1–9. CRC Press, 2015.